Experimental advances and preliminary mathematical modeling of the Swiss-roll mixed-reactant direct borohydride fuel cell

Amin Aziznia, Colin W. Oloman, Előd L. Gyenge*

Department of Chemical and Biological Engineering, Clean Energy Research Center, The University of British Columbia, 2360 East Mall, Vancouver, BC V6T 1Z3, Canada

HIGHLIGHTS

- Engineering advancements presented for the Swiss-roll mixed reactant borohydride–oxygen alkaline fuel cell.
- High power density (2500 W m^{-2}) and excellent durability demonstrated with Pt–Ag anode–cathode catalyst combination.
- The role of porous diaphragm separator and fluid distributor metallic mesh pore size is demonstrated.
- First preliminary mathematical model of the mixed reactant borohydride–oxygen fuel cell.

GRAPHICAL ABSTRACT
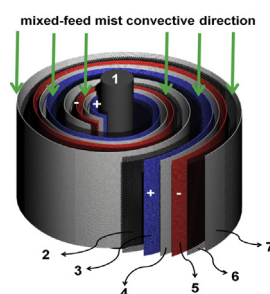
ABSTRACT

The Swiss-roll single-cell mixed reactant (SR-MRFC) borohydride – oxygen fuel cell equipped with Pt/carbon cloth 3D anode and either MnO$_2$ or Ag gas-diffusion cathodes is investigated by a combination of experimental studies and preliminary mathematical modeling of the polarization curve. We investigate the effects of four variables: cathode side metallic mesh fluid distributor, separator type (Nafion 112® vs. Viledon®), cathode catalyst (MnO$_2$ vs. Ag), and the hydrophilic pore volume fraction of the gas-diffusion cathode. Using a two-phase feed of alkaline borohydride solution (1 M NaBH$_4$ − 2 M NaOH) and O$_2$ gas in an SR-MRFC equipped with Pt/C 3D anode, MnO$_2$ gas diffusion cathode, Viledon® porous diaphragm, expanded mesh cathode-side fluid distributor, the maximum superficial power density is 2230 W m^{-2} at 323 K and 105 kPa(abs). The latter superficial power density is almost 3.5 times higher than our previously reported superficial power density for the same catalyst combinations. Furthermore, with a Pt anode and Ag cathode catalyst combination, a superficial power density of 2500 W m^{-2} is achieved with superior performance durability compared to the MnO$_2$ cathode. The fuel cell results are substantiated by impedance spectroscopy analysis and preliminary mathematical model predictions based on mixed potential theory.

© 2014 Elsevier B.V. All rights reserved.

1. Introduction

The conventional design of proton exchange membrane (PEM) fuel cell stacks is based on a plate-and-frame in series architecture that evolved from Volta's original concept of the zinc-air battery stack. The performance, durability and cost of the various

* Corresponding author.
E-mail address: egyenge@chbe.ubc.ca (E.L. Gyenge).

Nomenclature

a	electrode specific surface area (m^2 m^{-3})
$C_{BH_4^-}^{inlet}$	inlet concentration of sodium borohydride (mol m^{-3})
$C_{O_2}^{air}$	inlet concentration of oxygen in air (mol m^{-3})
$C_{O_2}^{inlet}$	inlet concentration of oxygen in O$_2$ (mol m^{-3})
C_{NaOH}^{inlet}	inlet concentration of NaOH (mol m^{-3})
C_i	concentration of component i (mol m^{-3})
$D_{BH_4^-}$	BH$_4^-$ diffusion coefficient (m^2 s^{-1})
$D_{BH_4^-}^{eff}$	effective BH$_4^-$ diffusion coefficient (m^2 s^{-1})
$E_{BOR\ 298\ K}^{\circ}$	standard potential of BOR at 298 K (V$_{SHE}$)
$E_{ORR\ 298\ K}^{\circ}$	standard potential of BOR at 298 K (V$_{SHE}$)
E_a	anode potential (V$_{SHE}$)
E_a^{OCP}	anode open circuit potential (V$_{MMO\ or\ SHE}$)
E_a^e	equilibrium potential of BOR (V$_{SHE}$)
E_c	cathode potential (V$_{SHE}$)
E_c^{OCP}	cathode open circuit potential (V$_{MMO\ or\ SHE}$)
E_c^e	equilibrium potential of ORR (V$_{SHE}$)
$E_{cell\ (j)}$	cell voltage at current density of j (V)
K_a	local mass transfer coefficient of anode (m s^{-1})
K_c	global cathode mass transfer coefficient (m s^{-1})
$K_{m,i}$	mass transfer coefficient of component i (m s^{-1})
P_{O_2}	partial pressure of oxygen in feed (kPa(abs))
$R_{contact}$	electronic plus contact resistance (Ohm m^2)
d_{cloth}	carbon cloth fiber diameter (m)
$j_{BOR_{MnO_2}}$	current density of BOR on MnO$_2$ (A m^{-2})
$j_{BOR_{Pt}}$	current density of BOR on Pt (A m^{-2})
$j_{L_{O_2}}^a$	limiting current density of ORR in anode (A m^{-2})
$j_{L_{air}}$	limiting current density of cathode in air (A m^{-2})
$j_{ORR_{MnO_2}}$	current density of ORR on MnO$_2$ (A m^{-2})
$j_{ORR_{Pt}}$	current density of ORR on Pt (A m^{-2})
$j_{o,BOR_{MnO_2}}$	apparent exchange current density of BOR on MnO$_2$ (A m^{-2})
$j_{o,BOR_{Pt}}$	apparent exchange current density of BOR on Pt (A m^{-2})
$j_{o,ORR_{MnO_2}}$	apparent exchange current density of ORR on MnO$_2$ (A m^{-2})
$j_{o,ORR_{Pt}}$	apparent exchange current density of ORR on Pt (A m^{-2})
$j_{L,i}$	limiting current density of component i (A m^{-2})
$j_{L,i}$	limiting current density of component i (A m^{-2})
j_{L,BH_4}	local limiting current density of BH$_4^-$ (A m^{-2})
j_L^a	effective BH$_4^-$ mass transfer limiting current density in 3D anode (A m^{-2})
j_L^c	limiting current density of O$_2$ cathode (A m^{-2})
j_e	ionic current density (A m^{-2})
j_{net}	net current density (A m^{-2})
j_s	electronic current density (A m^{-2})
n_{BOR}	number of electron transferred in BOR reaction (8)
n_{ORR}	number of electron transferred in ORR reaction (4)
n_{rds}^a	number of electron transferred in rate determining step of BOR
n_{rds}^c	number of electron transferred in rate determining step of ORR
t'	electro-active thickness of 3D electrode (m)
F	Faradic constant (96,485 C mol^{-1})
P	oxidant pressure (kPa(abs))
R	Universal gas constant (8.314 J mol^{-1} K^{-1})
T	temperature (K)
j	current density (A m^{-2})
t	time (s)

Symbols containing Greek letters

ΔV	potential drop in the anolyte under mass transfer control
ΔS_{BOR}	standard entropy change of BOR (J K^{-1} mol^{-1})
ΔS_{ORR}	standard entropy change of ORR (J K^{-1} mol^{-1})
$\Delta \phi_{R_{contact}}$	contact resistance voltage drop (V)
$\Delta \phi_{ACL}^{ionic}$	ionic Ohmic voltage drop across ACL (V)
$\Delta \phi_{GDE}^{ionic}$	ionic Ohmic voltage drop across GDE (V)
$\Delta \phi_{Ohm}$	total Ohmic voltage drop (V)
$\Delta \phi_{sep}$	Ohmic drop over separator (V)
$\alpha_{BOR}^{MnO_2}$	charge transfer coefficient of BOR on MnO$_2$
α_{BOR}^{Pt}	charge transfer coefficient of BOR on Pt
$\alpha_{ORR}^{MnO_2}$	charge transfer coefficient of ORR MnO$_2$
α_{ORR}^{Pt}	charge transfer coefficient of ORR on Pt
δ_{ACL}	carbon cloth thickness (m)
δ_{GDE}	gas diffusion electrode thickness (m)
δ_{sep}	separator thickness (m)
ε_{ACL}	ACL (carbon cloth) porosity
ε_{GDE}	GDE porosity
ε_d	diaphragm porosity
$\kappa_e^{298\ K}$	effective ionic conductivity of electrolyte at 298 K (mho m^{-1})
$\kappa_e^{323\ K}$	effective ionic conductivity of electrolyte at 323 K (mho m^{-1})
κ_e^T	effective ionic conductivity of electrolyte at temperature T (mho m^{-1})
κ_{eff}	effective electrolyte conductivity (mho m^{-1})
κ_{eff}^{ACL}	effective electrolyte conductivity in ACL
κ_{eff}^{GDE}	effective ionic conductivity of GDE (mho m^{-1})
κ_{eff}^{sep}	effective ionic conductivity of separator (mho m^{-1})
λ	volume fraction of liquid in ε_{ACL}
ν	scan rate (V s^{-1})
τ	hydrophilic pore fraction of ε_{GDE}
ω	liquid volumetric flow rate (m^3 s^{-1})

Abbreviations

3D	3-dimensional
ACL	anode catalyst layer
BOR	borohydride oxidation reaction
CE	counter electrode
CV	cyclic voltammetry
DBFC	direct borohydride fuel cell
EIS	electrochemical impedance spectroscopy
GDE	gas diffusion electrode
MMO	mercury/mercury oxide
MRFC	mixed-reactant fuel cell
OCP	open circuit potential
OCV	open circuit voltage
ORR	oxygen reduction reaction
PEM	proton/polymer exchange membrane
RE	reference electrode
RHE	reversible hydrogen electrode
SEM	scanning electron microscopy
SHE	standard hydrogen electrode
SR-MRFC	Swiss-roll mixed-reactant fuel cell
SS	stainless steel
WE	working electrode

conventional plate-and-frame PEM fuel cell stack components (membrane, electrodes, bipolar flow-field plates) in conjunction with the complex thermal and water management of PEM stacks, are some of the major challenges hampering the larger scale adoption of this technology. A simplified design that overcomes these challenges can potentially speed the commercialization of fuel cells.

In 2012, we introduced an innovative Swiss-roll architecture for mixed-reactant fuel cells both in monopolar and bipolar modes that can address some of the above-mentioned challenges of the PEM fuel cell technology by eliminating the ion exchange membranes and bipolar flow-field plates, while providing a lighter, more compact, cylindrical stack architecture [1—3]. In the Swiss-roll design, a flexible sandwich of electrodes and separators is rolled around an electrically conductive central axis to give a compact 3D electrode space for the fuel cell reactions. A liquid/gas mixture of fuel and oxidant is passed longitudinally through the reactor (i.e., parallel to the central mandrel), as the two fluids move along the porous cell(s) both the anode(s) and the cathode(s) are exposed to fuel and oxidant. In this situation the performance of the cell depends primarily on the selectivity for the desired oxidation and reduction reactions and secondarily on the electrical conductivity (electronic and ionic) of the cell components. Due to the presence of both fuel and oxidant on each electrode, mixed electrode potentials are inherently established. Imparting selectivity for the desired electrode reactions is a major objective of mixed reactant fuel cell research.

As proof-of-principle, we tested the Swiss-roll mixed-reactant fuel cell (SR-MRFC) design using a two-phase mixture of alkaline sodium borohydride solution and oxygen [1,2]. Sodium borohydride has received attention as a promising electrochemical fuel because it has a number of attractive physicochemical attributes, such as a high theoretical gravimetric energy density (9.3 kWh kg^{-1}), stability in a solid form and in concentrated alkaline solutions, and an innocuous complete oxidation product (i.e., $NaBO_2$) [4,5].

In our previous work we mainly focused on finding selective anode and cathode electrocatalyst combinations to improve the power output of the membrane-free SR-MRFC. [1,2,6] As anode electrocatalysts Pt, PtRu and Os were investigated, whereas for the oxygen reduction reaction Ag [2], MnO_2 [1,2] and Fe-aminoantipyrine (Fe-AAPyr) [6,7] were tested. A 20×10^{-4} m^2 geometric surface area SR-MRFC with Os—MnO_2 anode—cathode electrocatalyst pair was operated in monopolar single-cell mode at 323 K, 105 kPa(abs) to give a peak superficial power density of 1800 W m^{-2} [1]. The latter peak power matches the highest reported power densities for conventional dual chamber PEM direct borohydride fuel cells. These successful proof-of-principle investigations demonstrate the potential of the SR-MRFC and warrant further studies.

The present work combines experimental studies and preliminary mathematical modeling to advance the understanding of the cell polarization behavior of the Swiss-roll mixed reactant fuel cell operating with a mixture of alkaline sodium borohydride solution and oxygen gas. Mathematical modeling is important in the design and understanding of any electrochemical system. However, with respect to mixed-reactant fuel cells of any kind, there have been very few modeling studies published. In the present work, a preliminary mathematical model of the SR-MRFC polarization curve is presented for the mixed borohydride—oxygen system, based on mixed potential theory applied to both cathode and anode. The model also accounts for Ohmic potential losses and mass transfer overpotentials at the electrodes.

2. Experimental

The Swiss-roll design for mixed-reactant fuel cells was described in our previous reports [1,2]. Flexible layers composed of the anode, cathode, separator and metal mesh current collector/fluid distributors with 20×10^{-4} m^2 geometric area each (height: 0.02 m $\times$ width: 0.10 m), are tightly rolled around an electrically conductive mandrel that acts as the cathode current collector. The
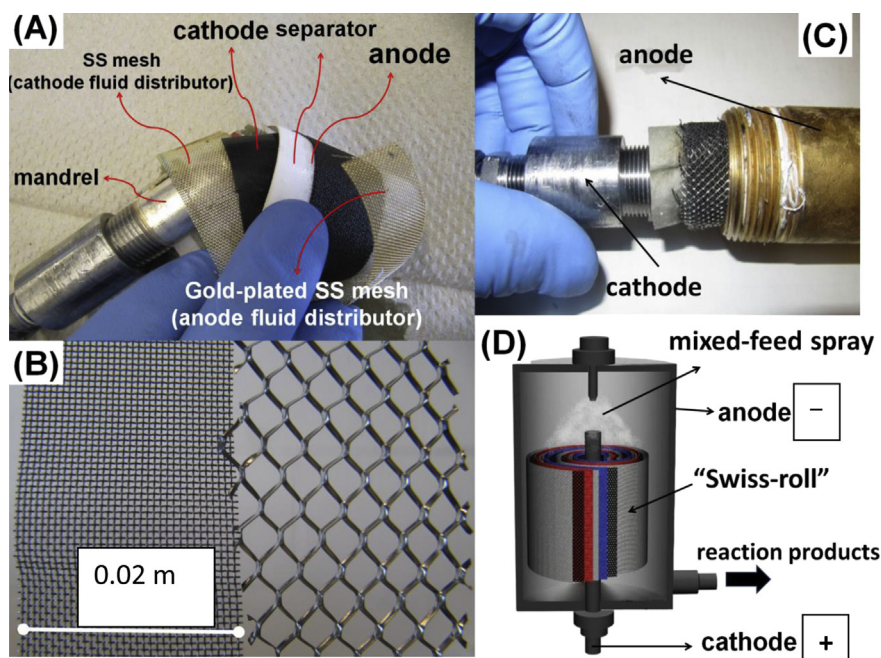

Fig. 1. Images of the (A) Swiss-roll components, (B) two different cathode fluid distributors/current collectors investigated in this work: stainless steel mesh #40 (left) and stainless steel expanded mesh #6 (right), (C) sliding the tightly rolled layers into the cell housing, and (D) Swiss-roll mixed-reactant fuel cell schematic with spray feeder (color online).
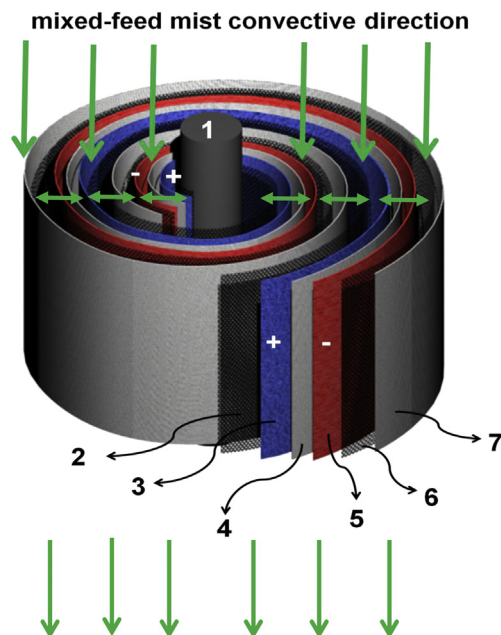
mixed-feed mist convective direction

Fig. 2. Schematic illustration of the Swiss-roll components and the flow of the reactant (alkaline borohdyride solution/oxygen gas) mist produced by the spray feeder. Legend: 1: stainless steel middle mandrel (cathode current collector), 2. Cathode stainless steel mesh fluid distributor/current collector, 3. Cathode GDE, 4 and 7. Separator (porous diaphragm Viledon®), 5: 3D anode (Pt/C on carbon cloth), 6. Anode Au-plated stainless steel mesh fluid distributor/current collector in electric contact with the cell housing. Note: only the anode current collector (6) is in electric contact with the cell housing.

rolled assembly is inserted under a tight fit in the cell housing with an inner diameter of 0.05 m (Fig. 1). The anode and the anode current collector/fluid distributor is in electric contact with the inner wall of the cell housing over an area of 0.02 × 0.01 m^2.

As separator, instead of the typically used ion-exchange membrane (e.g. Nafion), a porous diaphragm is used to provide the necessary electronic insulation while providing ionic conductivity between the adjacent electrode layers. The three-dimensional (3D) anode with Pt electrocatalyst was manufactured in-house by spraying the Pt/C catalyst ink onto a woven carbon cloth (Electro-Chem Inc., thickness: 350 μm) [2]. The Pt loading was 0.8 mg cm^{-2}. Two commercial oxygen (or air) gas diffusion electrodes (GDE) obtained from Gaskatel GmbH were employed as cathode: with MnO$_2$ (loading 15 mg cm^{-2}) or Ag (loading 20 mg cm^{-2}) catalyst, respectively. Fig. 1 shows the Swiss-roll components (A), the two types of cathode fluid distributors investigated (B), the tightly rolled assembly of layers being introduced in the cell housing (C) and a schematic representation of the Swiss-roll fuel cell equipped with a spray feeder (D). The layers composing the roll are cut to dimensions and rolled such as to avoid short-circuits between the cell housing and the cathode or the central mandrel and the anode respectively. The separator layer is also very important in this regard, to provide electronic insulation.

The Swiss-roll design does not employ any of the conventional flow-field/bipolar plates that are common in the PEM fuel cell industry for feeding and distributing the reactants to the electrodes. Instead, metallic porous fluid distributors are used with different hydrophobic/hydrophilic characteristics for the anode and cathode, respectively, to assure mass transfer selectivity in the mixed two-phase system. High retention of the liquid droplets is desired for the anode fluid distributor in order to keep the hydrophilic anode flooded with liquid anolyte (i.e., alkaline sodium borohydride solution), hampering the transport of gaseous oxygen to the anode. The cathode fluid distributor on the other hand, should provide

effective oxygen gas mass transfer to the cathode while minimizing the access of the liquid. In terms of the Laplace pressure across a gas/liquid interface in a capillary, there are two variables to consider: the three-phase contact angle and the capillary radius. The former is determined by the surface properties of the fluid distributor (e.g., surface composition and roughness). Generally clean metal surfaces are virtually perfectly wetted by aqueous solutions. Regarding the second variable, the pore size, the larger the pore the smaller is the Laplace pressure, hence, the lower is the gas breakthrough pressure. This is desirable in the present case for the cathode distributor. Hence, in this work on the cathode side two different fluid distributors were studied (Fig. 1(B)): (a) 304 stainless steel (SS) mesh #40 and (b) 316L expanded SS mesh #6 (Dexmet Corp., S67800/4SS(316L) 23-284DBA). The expanded mesh #6 has wider perforations and is expected to have higher gas hold-up in the pores compared to mesh # 40. On the anode side, a gold plated 304 stainless steel (SS) screen (Screen Technology Group Inc., mesh # 40, with 4 μm gold plated layer) was used with its geometric size matching that of the anode (height: 0.02 m × width: 0.10 m).

The Swiss-roll MRFC is operated with a two-phase liquid (fuel)/ gas (oxidant) mixture fed co-currently from the top, as shown conceptually in Fig. 1(D) and Fig. 2. The dispersion of the two-phase fluid is an important aspect of the Swiss-roll design that affects the performance of the fuel cell [3b,c]. The reactant mass transfer rates,
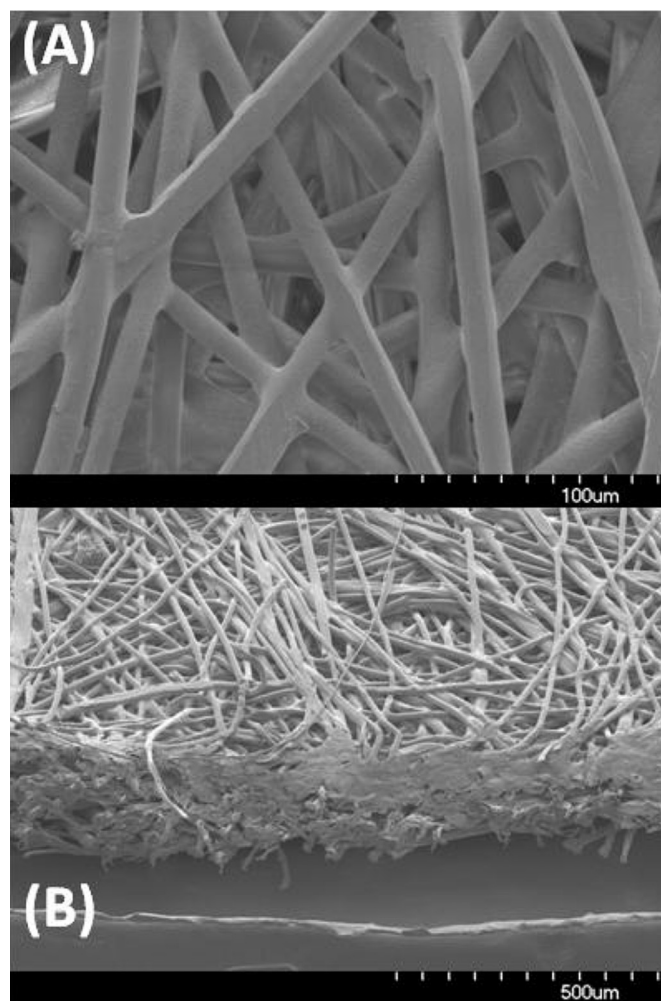

Fig. 3. Scanning electron microscopy images of the non-woven hydrophilic polyolefin diaphragm Viledon® used as separator in the SR-MRFC. Lengths scale: A) 100 μm, B) 500 μm.
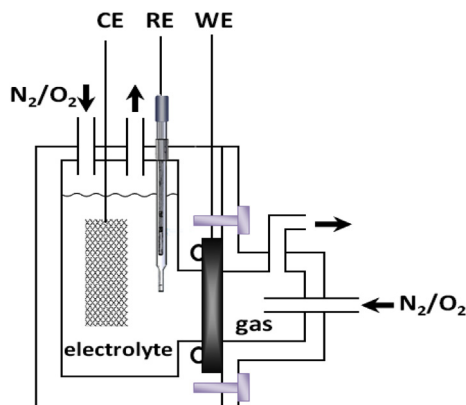
Fig. 4. Gas diffusion half-cell for electrode kinetics studies of the MnO$_2$ cathode.

temperature profile and parasitic power consumption are some of the engineering factors that depend on the fluid feeding device and the associated fluid dynamics in the cell. After initial work with a simple gas/liquid mixing tee, a gas driven liquid spray nozzle was adopted to feed the Swiss-roll reactor [3b,c]. The spray nozzle provides a uniform distribution of micron-size liquid (alkaline borohydride solution) droplets in the gas continuous phase [3b,c].

Fig. 2 shows the schematic of the axial convective mist flow generated by the spray feeder. In addition to axial dispersion and axial concentration gradients in the roll, there could be also radial dispersion and radial concentration gradients. The longer and wider the roll the more non-uniform is the two-phase flow distribution and the more significant are the concentration, temperature, potential and current gradients. In the present work the roll height was only 0.02 m therefore significant axial gradients are not expected. The spray nozzle angle of attack (in the present case 18°) and the nozzle tip distance from the roll (0.01 m) in relation to the roll width are important engineering design variables that can have a significant impact on the gas/liquid distribution. A complete fluid dynamic analysis of the mist (spray) flow in the Swiss-roll was beyond the objective here but nevertheless it is a very important goal for our future studies.

The separator used in this study was one layer of a hydrophilic polyolefine diaphragm (Viledon® FS2227E, Freudenberg Nonwovens Inc.) with thickness of 215 μm, 66% pore volume, and predominant pore radius of 10 μm (Fig. 3). Viledon® has excellent wetting property (wicking rate: 0.0075 m min^{-1} in 30% KOH at 293 K) and high electrolyte absorption (0.180 kg m^{-2}, 30% KOH) [8]. The separator prevents the cathode and anode from short-circuiting and it is non-selective toward ionic (i.e., BH$_4^-$, OH$^-$, and Na$^+$) permeability. For comparison, a proton-exchange membrane Nafion®-112 was also tested in the SR-MRFC and the results are discussed (see further).

To augment the modeling with relevant electrode kinetic data, the electrocatalytic activity of the MnO$_2$-based GDE for the oxygen reduction reaction (ORR) and its selectivity with respect to NaBH$_4$ oxidation were studied by half-cell experiments. The half-cell experiments were carried out in an asymmetric H-glass cell with a gas and an electrolyte chamber, respectively (Fig. 4). The working electrode (GDE), with geometrical surface area of 3.1×10^{-4} m^2, was placed between these two chambers and sealed with a rubber gasket. The gas chamber is provided with inlet and outlet ports for the gas flow. The whole assembly was placed in a heater for carrying out experiments at 323 K. A WaveNow potentiostat (Pine Research Instruments) was used to record the polarization curves and cyclic voltammograms. As reference and working electrodes, a Hg/HgO/0.1 M KOH electrode (XR400, Radiometer Analytical) and a

platinized titanium counter electrode were employed, respectively. All the electrode potentials in this work are referenced versus the mercury/mercury oxide (MMO) reference electrode. Before measurements, N$_2$ was sparged into the electrolyte for about 60 min to remove the dissolved oxygen from the electrolyte. Then O$_2$ was sparged for about 30 min. During half-cell polarization experiments, a flow of O$_2$ at ambient pressure (101 kPa (abs)) was maintained over the electrolyte surface and in the gas diffusion chamber.

Fuel cell experiments were conducted using the Fideris MTK test station. To determine the Ohmic resistance of the SR-MRFC, electrochemical impedance spectroscopy (EIS) was performed using a PARSTAT 2263 potentiostat (Princeton Applied Research). The EIS was measured at the open circuit voltage (OCV) with amplitude of 10 mV in the frequency range of 10^5 Hz to 10^{-2} Hz. For finding the contact resistance in the cell, the Swiss-roll was assembled without the separator (i.e., short-circuited from inside) and EIS was performed while there was no reactant or electrolyte inside the reactor. Since there was no ionic conductivity inside the reactor, the measured impedance was related to total electronic and contact resistances of the components.

3. Model development

With respect to mixed-reactant fuel cells of any kind, there have been very few modeling studies published [9]. In the present study, a mathematical model of the SR-MRFC is presented with respect to the borohydride–oxygen system. In contrast to other type of direct fuel cells, very few numerical models have been developed specifically for direct borohydride fuel cells [10–12]. Verma and Basu [11] developed a simplified model ignoring important cathode activation and mass-transfer overpotentials. A more detailed mathematical model was developed by Shah et al. [12] taking into account the mixed-potential on the anode due to hydrogen presence on the surface in conjunction with borohydride. However, all the previous models neglected the mixed-potential losses at the electrodes induced by simultaneous borohydride oxidation and oxygen reduction reactions (i.e., BOR and ORR). Thus, previous models implicitly assumed absence of fuel or O$_2$ crossover and perfectly selective anode and cathode electrocatalysts. Mixed-potential losses are important, not only for the SR-MRFC, but also for conventional DBFC with membrane separator (e.g. proton exchange membrane, PEM). At the cathode of a PEM DBFC, borohydride can cross-over through the membrane, similar to methanol cross-over in direct methanol fuel cells, lowering the Faradaic efficiency and the operating voltage of the DBFCs [13]. Mixed-potential losses are even more vital in the SR-MRFC due to the mixed-reactant operation of the fuel cell and must be estimated. Therefore, a simple preliminary model is developed in this work to gain insights in the SR-MRFC polarization behavior based on mixed potentials at the electrodes and also taking into account pertinent Ohmic losses and mass transfer effects.

The present model is limited as it applies only to an isobaric and isothermal single cell SR-MRFC operating at steady-state with constant reactant composition. These conditions are close to those of the present experimental work but would not apply in a larger scale fuel cell where electric potential, current, temperature and composition gradients in both axial and radial directions may be substantial. Further, this model assumes equipotential current feeders (i.e. zero voltage drops along the metal mesh) and neglects the electrooxidation of H$_2$ generated from the thermocatalytic decomposition of BH$_4^-$.

The model variables and their respective units are given in the Nomenclature. The experimental conditions for the model are:

Table 1
Variables and parameters used in the mathematical modeling of the SR-MRFC.

Symbol	Definition	Value	Unit	Note
Operating conditions				
P	O_2 pressure	105	kPa(abs)	
T	Temperature	323	K	
$C_{O_2}^{inlet}$	O_2 inlet concentration	39	mol m^{-3}	
$C_{O_2}^{air}$	Air inlet concentration	8	mol m^{-3}	
ω	Liquid flow rate	2×10^{-6}	m^3 s^{-1}	
$C_{BH_4}^{inlet}$	Inlet concentration of NaBH$_4$	1000	mol m^{-3}	
C_{NaOH}^{inlet}	Inlet concentration of NaOH	2000	mol m^{-3}	
Anodic related				
$E_{BOR\ 298\ K}^{\circ}$	Standard potential of BOR at 298 K	-1.24	V$_{SHE}$	[25]
E_a^{OCP}	Anode open circuit potential	-1.14	V$_{MMO}$	Measured[a]
ΔS_{BOR}	Standard entropy change of BOR	357.8	J mol^{-1} K^{-1}	[26]
α_{BOR}^{Pt}	BOR charge transfer coefficient on Pt	0.4	—	Measured
$\alpha_{BOR}^{MnO_2}$	BOR charge transfer coefficient on MnO$_2$	0.5	—	Measured
$j_{o,BOR_{MnO_2}}$	BOR exchange current density on MnO$_2$	4.26	A m^{-2}	Measured
$j_{o,BOR_{Pt}}$	BOR exchange current density on Pt	60	A m^{-2}	[27]
n_{BOR}	Number of electron transfer in BOR	8	—	
n_{rds}^a	Number of electron transfer in rate determining step of BOR	2	—	Assumed
δ_{ACL}	ACL (carbon cloth) thickness	300×10^{-6}	m	SEM
ε_{ACL}	ACL (carbon cloth) porosity	0.9	—	Measured
D_{BH_4}	BH$_4^-$ diffusion coefficient in 2 M NaOH	3.63×10^{-9}	m^2 s^{-1}	[28]
λ	Volume fraction of liquid in ε_{ACL}	0.8	—	Assumed
d_{cloth}	Carbon cloth fiber	10×10^{-6}	m	SEM
K_a	Local mass transfer coefficient of anode	5×10^{-6}	m s^{-1}	[29]
j_L^a	Overall limiting current density of 3D anode	23000	A m^{-2}	Calc.
Cathodic related				
$E_{ORR\ 298\ K}^{\circ}$	Standard potential of ORR at 298 K	0.40	V$_{SHE,\ 298\ K}$	[25]
E_c^{OCP}	Cathode open circuit potential	-0.24	V$_{MMO}$	Measured[a]
ΔS_{ORR}	Standard entropy change of ORR	-387	J mol^{-1} K^{-1}	[26]
$\alpha_{ORR}^{MnO_2}$	ORR charge transfer coefficient: MnO$_2$	0.6	—	Fitted
α_{ORR}^{Pt}	ORR charge transfer coefficient: Pt	0.3	—	[30]
$j_{o,ORR_{MnO_2}}$	ORR apparent exchange current density: MnO$_2$	0.49	A m^{-2}	Measured
$j_{o,ORR_{Pt}}$	ORR exchange current density: Pt	2.1×10^{-3}	A m^{-2}	[30]
n_{ORR}	Number of electron transfer in ORR	4	—	
n_{rds}^c	Number of electron transfer in rate determining step of ORR	1	—	Assumed
δ_{GDE}	Gas diffusion electrode thickness	3×10^{-4}	m	SEM
ε_{GDE}	GDE porosity	0.5	—	Assumed
τ	Hydrophilic pore fraction of ε_{GDE}	—	—	Modeled
K_c	Apparent cathode mass transfer coefficient	10^{-3}	m s^{-1}	Calc.
j_L^c	Limiting current density of the O$_2$ cathode	15000	A m^{-2}	Calc.
Separator & electrolyte				
$\kappa_e^{298\ K}$	Ionic conductivity of electrolyte at 298 K	32.7	mho m^{-1}	[24]
$\kappa_e^{eff/sep}$	Effective ionic conductivity of separator	12.1	mho m^{-1}	
ε_d	Separator (diaphragm) porosity	0.66	—	
δ_{sep}	Separator thickness	1.8×10^{-4}	m	
Swiss-roll components				
$\sum R_{contact}$	Total Ohmic resistance of the Swiss-roll	4×10^{-6}	Ohm m^2	Measured

[a] Note: Open circuit potentials of electrodes were measured using a Hg/HgO reference electrode (MMO).

MnO$_2$ gas diffusion cathode and three-dimensional Pt/carbon cloth anode. Table 1 summarizes the model parameters.

3.1. Equilibrium electrode potentials

At the anode of a DBFC, borohydride ions are oxidized on the electrocatalyst surface ideally in an eight-electron reaction:

$$BO_2^- + 6H_2O + 8e^- \leftarrow BH_4^- + 8OH^- \left(E_{BOR\ 298\ K}^0 = -1.24 V_{SHE} \right) \tag{1}$$
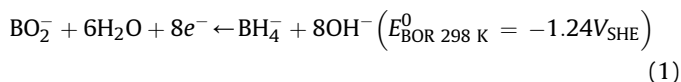
The equilibrium potential of Eq. (1) can be calculated from the Nernst equation (Eq. (2)) where the activities of the species are approximated with the molar concentration (ideal solution assumption):

$$E_a^e = E_{BOR\ 298\ K}^{\circ} + \frac{\Delta S_{BOR}}{8F}(T - 298) - \frac{RT}{8F} ln \left(\frac{[BH_4^-][OH^-]^8}{[BO_2^-]} \right) \tag{2}$$

The electro-oxidation of BH$_4^-$ has been extensively investigated over the last decade. In experimental and theoretical studies it has been shown that the electro-oxidation of BH$_4^-$ involves a number of competitive electrocatalytic and thermocatalytic pathways, that can diminish the Faradaic equivalence from eight to four electrons per BH$_4^-$ converted, depending on the electrocatalyst, electrode potential, temperature and OH$^-$/BH$_4^-$ concentration ratio [14–21].

The non-Faradaic hydrolysis of BH$_4^-$ (Eq. (3)) catalyzed by surfaces such as Pt and Ru, generates H$_2$ that may be oxidized in-situ (Eq. (4)) and/or released as gas bubbles [17]. The H$_2$ gas bubbles interfere with mass transport in the anode (i.e. gas evolving electrode) and also lower the effective anolyte ionic conductivity in the porous anode.

$$BH_4^- + 2H_2O \rightarrow BO_2^- + 4H_2 \tag{3}$$

$$2H_2O + 2e^- \leftarrow H_2 + 2OH^- \left(E_{298}^0 = -0.83 V_{SHE} \right) \tag{4}$$
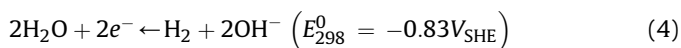
In the presence of BH$_4^-$ hydrolysis, the electrooxidation mechanism at the anode is complicated and it is not fully understood at

this time. Shah et al. presented a model involving both H_2 and BH_4^- oxidations (BOR) on the anode. [12] In the present model, we consider the mixed-potential due to borohydride oxidation and oxygen reduction (ORR) on the anode surface. However, for the sake of simplicity, the contribution of the competitive H_2 oxidation is neglected. Furthermore, we also took into account the mixed-potential on the MnO_2 gas diffusion cathode due to simultaneous ORR and BOR.

The ORR is given by Eq. (5):

$$O_2 + 2H_2O + 4e^- \rightarrow 4OH^- \quad \left(E_{ORR\ 298\ K}^0 = 0.40 V_{SHE}\right) \tag{5}$$
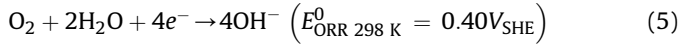
The equilibrium ORR potential is expressed by Eq. (6):

$$E_c^e = E_{ORR\ 298\ K}^\circ + \frac{\Delta S_{ORR}}{4F}(T - 298) - \frac{RT}{4F} ln\left(\frac{[OH^-]^4}{P_{O_2}}\right) \tag{6}$$

3.2. Activation overpotentials

For the anodic and cathodic reaction, the dependence of activation overpotentials on current density is determined by the Erdey-Grúz−Volmer−Butler equations:
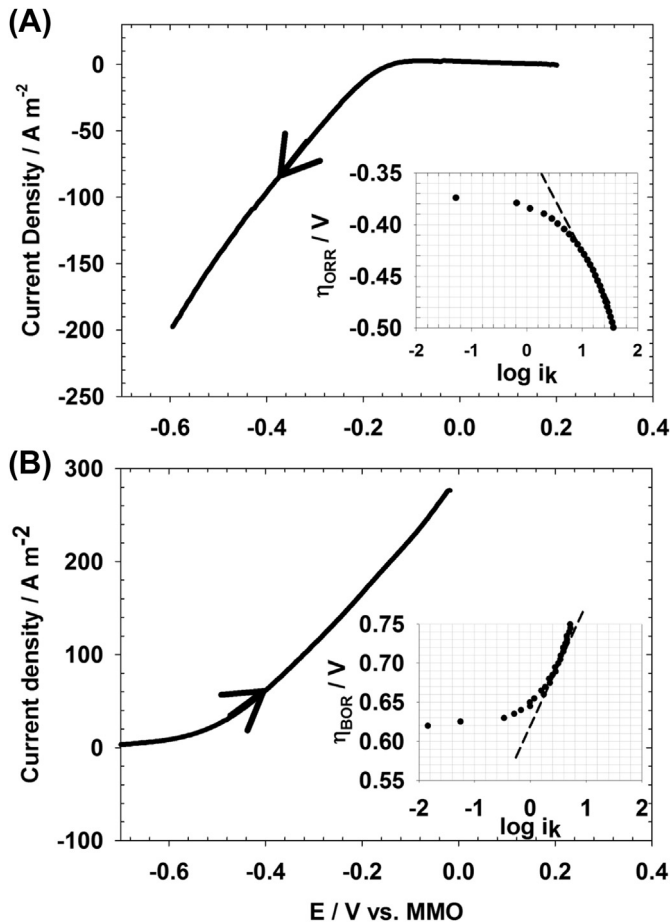
(A)

(B)

Fig. 5. Linear voltammetry and Tafel plot (inset) of the MnO_2 gas-diffusion electrode for (A) oxygen electroreduction in 2 M NaOH and (B) borohydride oxidation in 2 M NaOH − 1 M NaBH$_4$ N$_2$-purged electrolyte. Temperature: 333 K, Pressure: 101.3 kPa (abs), Scan rate 5 mV s^{-1}. Note: the net current densities are shown, i.e., after subtraction of the baseline MnO_2 response in N$_2$-purged 2 M NaOH. $E_{BOR}^e = -1.40$ V$_{MMO}$ and $E_{ORR}^e = 0.21$ V$_{MMO}$.

$$j_{BOR_{Pt}} = j_{o,BOR_{Pt}} \left(\exp\left(\frac{\alpha_{BOR}^{Pt} n_{rds}^a F(E_a - E_a^e)}{RT}\right) - \exp\left(\frac{-(1 - \alpha_{BOR}^{Pt}) n_{rds}^a F(E_a - E_a^e)}{RT}\right) \right) \tag{7}$$

$$j_{ORR_{MnO_2}} = j_{o,ORR_{MnO_2}} \left(\exp\left(\frac{\alpha_{ORR}^{MnO_2} n_{rds}^c F(E_c - E_c^e)}{RT}\right) - \exp\left(\frac{-(1 - \alpha_{ORR}^{MnO_2}) n_{rds}^c F(E_c - E_c^e)}{RT}\right) \right) \tag{8}$$

In order to determine the transfer coefficients and the exchange current densities separate half-cell polarization experiments were performed with electrodes and electrolytes identical to those used in the fuel cell experiments (see further). Table 1 presents the values of these electrode-kinetic parameters. Fig. 5 shows half-cell polarization experiments used to extract pertinent kinetic data for ORR on MnO_2 and to investigate the selectivity of MnO_2 cathode toward BOR (for discussion, see further).

3.3. Mixed-potential

In the SR-MRFC, the potentials at the anode and cathode are mixed-potentials due to the simultaneous occurrence of BOR and ORR. Considering the Erdey-Grúz−Volmer−Butler equation for BOR and ORR, the anode and cathode mixed-potentials (i.e., E_a^{OCP}, E_c^{OCP}) at net zero superficial current density are calculated from Eqs. (9)−(10)):

$$j_{o,BOR_{Pt}} \left(\exp\left(\frac{\alpha_{BOR}^{Pt} n_{rds}^a F\left(E_a^{OCP} - E_a^e\right)}{RT}\right) - \exp\left(\frac{-(1 - \alpha_{BOR}^{Pt}) n_{rds}^a F\left(E_a^{OCP} - E_a^e\right)}{RT}\right) \right)$$
$$= j_{o,ORR_{Pt}} \left(\exp\left(\frac{\alpha_{ORR}^{Pt} n_{rds}^c F\left(E_a^{OCP} - E_c^e\right)}{RT}\right) - \exp\left(\frac{-(1 - \alpha_{ORR}^{Pt}) n_{rds}^c F\left(E_a^{OCP} - E_c^e\right)}{RT}\right) \right) \tag{9}$$

$$j_{o,BOR_{MnO_2}} \left(\exp\left(\frac{\alpha_{BOR}^{MnO_2} n_{rds}^c F\left(E_c^{OCP} - E_a^e\right)}{RT}\right) - \exp\left(\frac{-\left(1 - \alpha_{BOR}^{MnO_2}\right) n_{rds}^c F\left(E_c^{OCP} - E_a^e\right)}{RT}\right) \right)$$
$$= j_{o,ORR_{MnO_2}} \left(\exp\left(\frac{\alpha_{ORR}^{MnO_2} n_{rds}^c F\left(E_c^{OCP} - E_c^e\right)}{RT}\right) - \exp\left(\frac{-\left(1 - \alpha_{ORR}^{MnO_2}\right) n_{rds}^c F\left(E_c^{OCP} - E_c^e\right)}{RT}\right) \right) \tag{10}$$

3.4. Mass-transfer limited current density

The mass-transfer limited current density is defined as:

$$j_{L,i} = nFK_{m,i}C_i \quad i = O_2, NaBH_4 \tag{11}$$

For the anode, considering that the carbon cloth is the only region imposing mass transport limitations and that no convective flow occurs in the pores of the carbon cloth, the local BH_4^- mass transport limiting current density can be estimated by Ref. [22]:

$$j_{L,BH_4} = 8FK_a C_{BH_4^-}^{\text{inlet}} \qquad (12)$$

The numbers of electrons exchange per BH_4^- anion during oxidation on Pt is less than the theoretical eight-electrons, the literature suggests typically between four to six-electrons exchanged. However, as indicated before, in order to simplify the model, the complex details of the BH_4^- electro-oxidation mechanism leading to incomplete oxidation products and pathways are neglected.

The local BH_4^- mass transport coefficient to the fiber surface in the carbon cloth anode K_a is also affected by the inherent H_2 gas evolution generated by BH_4^- hydrolysis. The mass transfer situation is similar to the case of methanol mass transfer in a direct methanol fuel cell anode with CO_2 gas evolution studied by Scott et al. [29] Hence, based on the study by Scott et al. we estimated K_a to be 5×10^{-6} m s^{-1} giving a local BH_4^- mass transfer limiting current density of approximately 3800 A m^{-2}.

The SR-MRFC uses a 3D anode (Pt/C on carbon cloth). The overall mass transfer limited current density in a 3D anode is calculated by taking into account both the specific surface area and the electro-active thickness to express the actual mass transfer capacity of the electrode [23,24]. The electro-active thickness of the 3D anode can be determined by Eq. (13) [23,24]:

$$t' = \sqrt{\frac{2\Delta V \kappa_{\text{eff}}^{\text{ACL}}}{a j_{L,i}}} \qquad (13)$$

Where $\kappa_{\text{eff}}^{\text{ACL}}$ is the effective electrolyte conductivity in the anode catalyst layer (ACL). Due to the generation of H_2 bubbles at the anode surface (as a result of BH_4^- hydrolysis over Pt) the carbon cloth contains a volume fraction of gas. Therefore, to estimate $\kappa_{\text{eff}}^{\text{ACL}}$ with a Bruggeman type of equation, it is necessary to assume the liquid volume fraction in the porous anode, λ:

$$\kappa_{\text{eff}}^{\text{ACL}} = (\varepsilon_{\text{ACL}}\lambda)^{\frac{3}{2}} \kappa_e^T \qquad (14)$$

Where κ_e^T is the electrolyte conductivity at the operating temperature. It is not possible to measure the volume fraction of liquid in the carbon cloth during operation. Assuming a liquid volume fraction of 0.8, with a BH_4^- concentration of 1 M and $\Delta V = 0.1$ V (i.e. typical potential drop across the ACL under mass transfer control), the electro-active thickness of the SR-MRFC is calculated with Eq. (13) to be 150×10^{-6} m, which indicates that about half of the geometric thickness of the 3D anode (carbon cloth) is electrochemically active under mass transfer limiting conditions.

The effective mass transfer limiting current density of BH_4^- in the 3D anode can be then calculated by Eq. (15):

$$j_L^a = a t' j_{L,BH_4} \qquad (15)$$

Where a is the electrode specific surface area (m^2 m^{-3}) and for the carbon cloth anode substrate can be estimated by Ref. [24]:

$$a = \frac{4(1 - \varepsilon_{\text{ACL}})}{d_{\text{cloth}}} \qquad (16)$$

With ε_{ACL} of 0.9 and d_{cloth} of 10×10^{-6} m, the specific surface area of the 3D anode was determined to be 4×10^4 m^2 m^{-3}.

Therefore j_L^a, the overall limiting current density of the 3D anode, is estimated as ca. 23000 A m^{-2}. Due to the high mass transfer capacity of the 3D anode, the effective BH_4^- mass limiting current density is high and it is unlikely to be the overall limiting factor in the operation of the SR-MRFC.

For the cathode GDE, the mass transfer coefficient was estimated by comparing the polarization performance of the SR-MRFC under air and oxygen at similar operating conditions Fig. 6(B)). The limiting current density of the SR-MRFC operated with air was determined (3000 A m^{-2}, Fig. 6(B)) and the apparent (overall) O_2 gas mass transport coefficient in the cathode was then calculated using Eq. (17) and reported in Table 1:

$$j_{L_{\text{air}}} = -4FK_c C_{O_2}^{\text{air}} = -4FK_c \frac{p_{O_2}}{RT} \qquad (17)$$

3.5. Ohmic losses

The development of SR-MRFC with low electrical resistance is a major challenge. The internal resistance can be lowered by, for instance, decreasing the inter-electrode gap and increasing the electrolyte conductivity. The Ohmic losses in this model include electronic and contact resistances of the current collectors and electrodes, and ionic losses in the separator anode catalyst layer, and the cathode GDE.

The ionic Ohmic drop across the porous separator can be written in terms of the effective ionic conductivity of the NaOH in separator and the current density:

$$\Delta\phi_{\text{sep}} = \frac{\delta_{\text{sep}}}{\kappa_{\text{eff}}^{\text{sep}}} j \qquad (18)$$

In a diaphragm of non-conducting material saturated by electrolyte, the effective ionic conductivity of the NaOH can be estimated by the Maxwell equation [24]:

$$\kappa_{\text{sep}}^{\text{eff}} = \frac{2\kappa_e^T \varepsilon_d}{3 - \varepsilon_d} \qquad (19)$$

The effect of the temperature on the ionic conductivity of NaOH is estimated by Ref. [24]:

$$\kappa_e^T = \kappa_e^{298 \text{ K}}(1 + 0.023(T - 298)) \qquad (20)$$

In the cathode GDE, the hydrophobic/hydrophilic balance of the pore network is essential for creation of an efficient three-phase reaction interface. To estimate the effective ionic conductivity of the electrolyte in the cathode GDE with a Bruggeman type of equation, it is necessary to introduce the hydrophilic pore volume fraction, τ:

$$\kappa_{\text{eff}}^{\text{GDE}} = (\varepsilon_{\text{GDE}}\tau)^{\frac{3}{2}} \kappa_e^T \qquad (21)$$

The total current density in the GDE is a combination of the electronic and ionic current densities:

$$j = j_s + j_e \qquad (22)$$

Usually pertinent differential equations must be solved to find the electronic and ionic current densities. However, in this model it is assumed that the entire cathode GDE is electrochemically active and the average electronic and ionic current densities in the cathode GDE are equal:

$$\frac{j}{2} = j_s = j_e \qquad (23)$$

A detailed analysis for the above simplifying assumption has been described by Shah et al. [12].

Therefore, the ionic Ohmic loss of the GDE then can be calculated with:

$$\Delta\phi_{GDE}^{ionic} = \frac{\delta_{GDE}}{\kappa_{eff}^{GDE}}\frac{j}{2} \tag{24}$$

the net anodic and cathodic superficial current densities must be equal in absolute values to the cell superficial current density:

$$j_{BOR_{Pt}} + j_{ORR_{Pt}} = j_{BOR_{MnO_2}} + j_{ORR_{MnO_2}} = j. \tag{28}$$

Each of the current densities in Eq. (28) can be expressed as mixed-control: charge transfer and mass transport, current densities, using:

$$\frac{1}{j_{BOR_{Pt}}} = \frac{1}{j_{o,BOR_{Pt}}\left(\exp\left(\frac{\alpha_{BOR}^{Pt}n_{rds}^a F(E_a - E_a^e)}{RT}\right) - \exp\left(\frac{(1-\alpha_{BOR}^{Pt})n_{rds}^a F(E_a - E_a^e)}{RT}\right)\right)} + \frac{1}{j_{L_{BH_4}}} \tag{29}$$

$$\frac{1}{j_{ORR_{Pt}}} = \frac{1}{j_{o,ORR_{Pt}}\left(\exp\left(\frac{\alpha_{ORR}^{Pt}n_{rds}^c F(E_a - E_c^e)}{RT}\right) - \exp\left(\frac{-(1-\alpha_{ORR}^{Pt})n_{rds}^c F(E_a - E_c^e)}{RT}\right)\right)} + \frac{1}{j_{L_{O_2}}^a} \tag{30}$$

$$\frac{1}{j_{ORR_{MnO_2}}} = \frac{1}{j_{o,ORR_{MnO_2}}\left(\exp\left(\frac{\alpha_{ORR}^{MnO_2}n_{rds}^c F(E_c - E_c^e)}{RT}\right) - \exp\left(\frac{-(1-\alpha_{ORR}^{MnO_2})n_{rds}^c F(E_c - E_c^e)}{RT}\right)\right)} + \frac{1}{j_{L_{O_2}}} \tag{31}$$

$$\frac{1}{j_{BOR_{MnO_2}}} = \frac{1}{j_{o,BOR_{MnO_2}}\left(\exp\left(\frac{\alpha_{BOR}^{MnO_2}n_{rds}^a F(E_c - E_a^e)}{RT}\right) - \exp\left(\frac{-(1-\alpha_{BOR}^{MnO_2})n_{rds}^a F(E_c - E_a^e)}{RT}\right)\right)} + \frac{1}{j_{L_{BH_4}}} \tag{32}$$

Similarly, to estimate the effective ionic conductivity in the 3D anode with a Bruggeman type of equation, it is necessary to take into account the liquid volume fraction λ in the 3D anode:

$$\kappa_{ACL}^{eff} = (\varepsilon_{ACL}\lambda)^{\frac{3}{2}}\kappa_e^T \tag{25}$$

The effective ionic potential drop in the 3D anode can be estimate by:

$$\Delta\phi_{ACL}^{ionic} = \frac{\delta_{ACL}}{\kappa_{eff}^{ACL}}\frac{j}{2} \tag{26}$$

The voltage loss due to the all the contact resistances can be calculated using Ohm's law:

$$\Delta\phi_{R_{contact}} = \frac{j}{2}\sum R_{contact} \tag{27}$$

The total contact resistance of the SR-MRFC components was measured according to a method described in the Experimental Section and is reported in Table 1.

3.6. Modeling approach

The model applies to an isobaric and isothermal single cell SR-MRFC operating at steady-state with fixed reactant compositions. These conditions are close to those of the present laboratory cell but would not apply for an industrial scale SR-MRFC where pressure, temperature and composition gradients may be substantial. Further, this model assumes uni-potential current feeders and neglects both the electro-oxidation of H$_2$ from the thermocatalytic decomposition of BH$_4^-$ and the possible incomplete electro-oxidation of BH$_4^-$.

With these caveats, our modeling approach was as follows: at non-zero current densities, conservation of charge demands that

The cell voltage is calculated from:

$$E_{cell} = E_c - E_a - \Delta\phi_{sep} - \Delta\phi_{GDE}^{ionic} - \Delta\phi_{ACL}^{ionic} - \Delta\phi_{R_{contact}} \tag{33}$$

All terms in Eq. (33) have been defined in previous sections. At a given cell voltage (E_{cell}), Equations (28)–(33) can be solved numerically and the SR-MRFC polarization curve is simulated. Variables and parameters of the Swiss-roll fuel cell components used in the model are shown in Table 1.

4. Results and discussion

The intrinsic electrocatalytic and mass transfer selectivities of the electrodes are paramount for the operation of mixed-reactant fuel cell systems. The ORR selectivity of manganese oxide-based electrocatalysts in the presence of the BH$_4^-$ has been studied previously [31,32]. Chatenet et al. reported that manganese oxide-based electrocatalysts (MnO$_x$/C, composition and crystal phase not mentioned) have excellent selectivity toward ORR in 1 M NaOH [31a]. In the presence of 0.01 M NaBH$_4$, they reported that the open circuit potential for MnO$_x$/C is decreased by only 0.075 V [31a]. Garcia studied the effect of different carbon supports on ORR selectivity of manganese oxide electrocatalysts and observed that the electrocatalyst supported on Monarch1000 carbon is BH$_4^-$ tolerant, whereas electrocatalysts supported on M225 and E350 carbon showed poor ORR selectivity [31b]. Furthermore, Sljukic et al. observed that the ORR activity of MnO$_2$/activated carbon electrocatalysts prepared by high temperature calcinations (593 K) is significantly suppressed in the presence of 0.5 M NaBH$_4$ whereas the electrocatalysts prepared by low temperature calcinations (393 K) still showed high activity and selectivity for the ORR [32]. In this work we used a commercial MnO$_2$ electrode (see Experimental Section), therefore, we performed a series of half-cell experiments

for both ORR and BOR in order to obtain the pertinent electrode kinetic parameters utilized in the mathematical model (Fig. 4).

The polarization curve for ORR on MnO_2 at 323 K is shown by Fig. 5. The ORR onset potential is -0.1 V_{MMO}. The Tafel plot generated from the polarization curve is presented by Fig. 5(A) (inset). We used the linear portion of the Tafel plot as depicted in Fig. 5(A), to obtain the ORR transfer coefficient and the exchange current density employed in the model and presented by Table 1. Thus, an ORR Tafel slope on MnO_2 of 106.7 mV dec^{-1} was determined at 323 K, corresponding to a transfer coefficient of 0.6. The exchange current density was 0.49 A m^{-2}. Gyenge and Drillet reported ORR transfer coefficients on various MnO_2 gas diffusion electrodes between 1.2 and 0.7 in 6 M KOH [33]. The more sluggish ORR observed in the present work, could be due a number of factors, such as the OH^- concentration difference (6 M KOH [33] vs. 2 M NaOH), different crystallographic features of the MnO_2 surface and differences in catalyst dispersion.

For ORR on Pt/C in 1 M KOH Yu et al. at 333 K reported two transfer coefficient regions (or Tafel slope regions): transfer coefficient of 0.3 (at high overpotentials) and 0.9 (at low overpotentials), respectively [30]. In our work, ORR on the Pt anode is considered in conjunction with BOR giving rise to the mixed anode potential. Due to the expected anode potential ranges, to model the ORR on the Pt anode we used the high overpotential ORR transfer coefficient and exchange current density presented by Yu et al. (Table 1) [30].

With respect to $NaBH_4$ electro-oxidation on the MnO_2 electrode, Fig. 5(B) shows the corresponding half-cell polarization curve. The MnO_2 has some electrocatalytic activity toward BH_4^- oxidation, the onset oxidation potential is -0.6 V_{MMO}. Hence, clearly a mixed potential must be considered on the cathode as well. The charge transfer coefficient and the exchange current density for BOR at 323 K on MnO_2 were determined from the corresponding Tafel plot (Fig. 5(B) inset) and are presented in Table 1.

With regard to mass transfer selectivity, flooding of the gas diffusion cathode by the alkaline borohydride solution could be a problem. Some commonly employed methods that could suppress cathode flooding are: (a) enhancing the hydrophobicity of the cathode and (b) optimizing the gas/liquid load ratio. In addition, the physical characteristics of the fluid distributors (Fig. 1) could play an important role in controlling the electrode flooding and assuring optimal reactant mass transfer to the electrodes. On the cathode side, as shown in Fig. 1(B), two types of stainless steel meshes, expanded mesh #6 and mesh #40, were tested with otherwise similar conditions. The expanded mesh #6 with wider openings improved considerably the SR MRFC polarization performance in the mass transfer control region, i.e., at current densities higher than 2500 A m^{-2} (Fig. 6(A)).

This result can be explained by the lower Laplace pressure (i.e., equilibrium interfacial pressure difference between the gas and liquid phases) in the larger pores of the expanded mesh #6, which allows for higher gas hold-up and improved oxygen mass transfer to the cathode. In contrast, when mesh # 40 was used (with smaller openings), severe oxygen mass transfer limitation occurred as a result of high liquid hold-up in the fine pores of the fluid distributor. The peak superficial power density of the SR MRFC with Pt–MnO_2 electrode pair and expanded mesh #6 cathode fluid distributor reached 2230 W m^{-2}, which is higher than any peak superficial power density ever reported for low temperature (<373 K) mixed-reactant fuel cells and matches the highest power densities of DBFCs with conventional PEM architecture.

Fig. 6(B) compares the performance of the SR-MRFC with expanded mesh #6 fluid distributor and Pt–MnO_2 electrode pair under oxygen and air, respectively, with otherwise similar condition. The open circuit voltages (OCV) with air and pure oxygen are
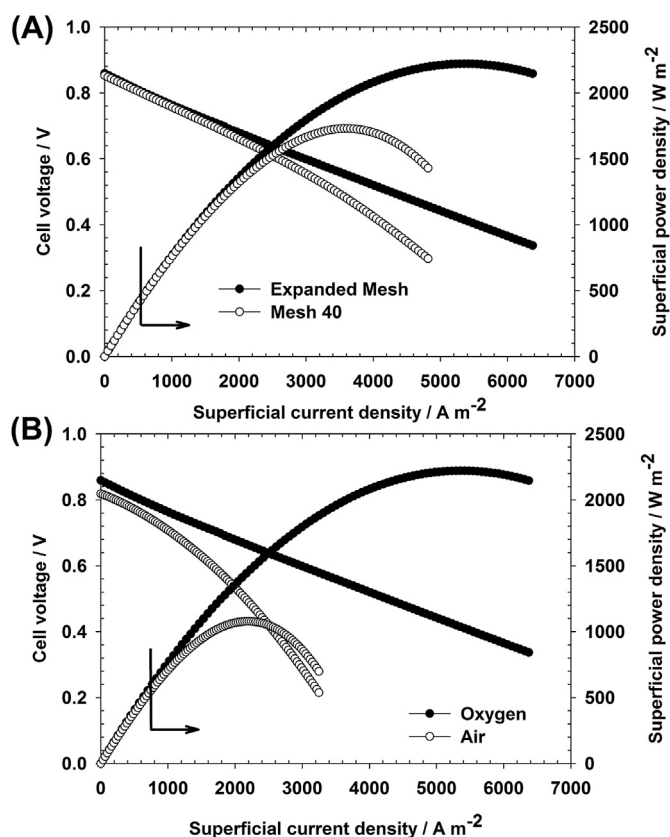

Fig. 6. (A) Effect of cathode fluid distributor on the SR-MRFC polarization: stainless steel mesh #40 and Stainless steel expanded mesh #6, (B) Effect of the oxidant on the polarization behavior of the SR-MRFC equipped with expanded mesh #6 cathode fluid distributor. Catalysts: anode (Pt/C loading 0.8 mg cm^{-2}), cathode commercial MnO_2 GDE (Gaskatel GmbH., 15 mg cm^{-2} MnO_2). Separator: Viledon®. Feed: 1 M $NaBH_4$ – 2 M NaOH (12 mL min^{-1}), O_2 (10 SL min^{-1}), 323 K, 105 kPa(abs).

respectively, 0.83 V and 0.86 V. When operated with air, the SR-MRFC can reach a maximum current density of 3500 A m^{-2}, which corresponds to oxygen mass transfer limitation. With pure oxygen on the other hand, no significant mass transport limitation was observed even at a current density of 6500 A m^{-2} (Fig. 6(B)).

Fig. 7 compares the polarization performance of a single cell SR-MRFC fed with oxygen on the cathode side using either Nafion®-112 or Viledon® as separator. Viledon® is a non-selective porous diaphragm as described in the Experimental Methods section. Fig. 7(A) shows the effect of the separator type on the cell impedance at the open-circuit voltage, whereas Fig. 7(B) compares the cell polarization performances. The open circuit voltages for Nafion® and Viledon® were respectively ca. 0.91 V and 0.86 V, whereas the corresponding peak superficial power densities were 1930 W m^{-2} and 2230 W m^{-2} (Fig. 7(B)). This difference in performance is attributed to the combined effects of mixed-potentials and ionic conductivity; both are dependent on the properties of the separator.

In particular, the peak superficial power density appears to depend mainly on the internal resistance of the fuel cell, which for the Nafion® 112 and Viledon® were: 0.042 Ω (8.4×10^{-5} Ω m^2) and 0.027 Ω (5.4×10^{-5} Ω m^2), respectively (Fig. 7(A) inset). The ionic conductivity of the Viledon® separator relies on the migration of all the ions present in the electrolyte through the non-selective porous matrix, in contrast to Nafion® that selectively transfers mostly the Na^+ only. The superior performance of the hydrophilic polymer separators over PEMs has been also shown in conventional DBFCs architectures with selective electrodes [34].
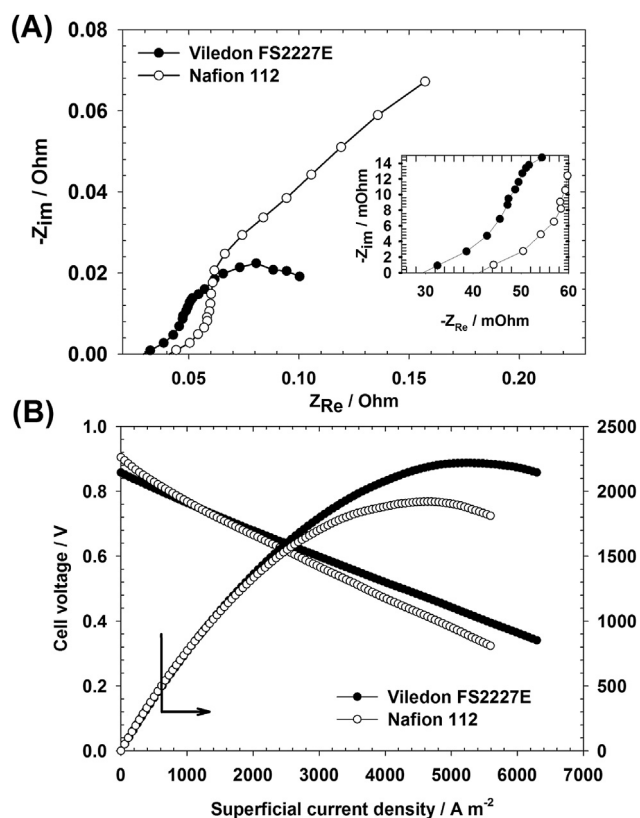
Fig. 7. (A) Impedance spectra at open circuit voltage of the SR-MRFC equipped with Nafion®-112 or Viledon® separators, respectively. Inset shows the high frequency data points. (B) SR-MRFC polarization comparison between Nafion®-112 and Viledon®, respectively. Pt/C anode, MnO₂/C cathode, expanded metal mesh #6 cathode fluid distributor. Other conditions are the same as in Fig. 6.

Fig. 8. Mathematical modeling of the SR-MRFC performance: (A) effect of the MnO₂ gas-diffusion cathode hydrophilic pore volume fraction τ, and (B) comparison with experimental data: Simulation with $\tau = 65\%$; experimental condition as in Fig. 6 (color online).

Furthermore, as shown by Fig. 7(A) the impedance spectra are strongly influenced by the separator type, i.e., either cation exchange membrane (Nafion® 112) or porous diaphragm (Viledon®). In case of the latter, the spectrum is of a semi-circle shape at lower frequencies, which is very similar to the spectra presented by Bidault et al. for oxygen (or air) gas diffusion cathodes in alkaline media and is described by the parallel combination of a constant phase element and a resistor [35,36]. When Nafion® 112 is employed, the spectrum at lower frequencies is fairly linear and it is similar to a typical impedance response of the Nafion® membrane (Na⁺ saturated) at the equilibrium potential, reported by Samec et al. [37]. According to Samec et al. this type of impedance spectra is due to the ion transport kinetic processes in the membrane pores and is essentially a Warburg-type impedance [37].

The comparative fuel cell polarization curves with the two different separators (Fig. 7(B)), support the impedance analysis by showing a higher Ohmic potential drop in case of Nafion®112, whereas when Viledon® was used, the Ohmic potential drop was lower but the potential drop was more pronounced in the kinetic region. Hence, the maximum superficial power density, which occurs at current densities in the Ohmic controlled region of the polarization curve, was higher for Viledon®, reaching 2230 W m⁻² (Fig. 7(B)). Therefore, the Viledon® separator was retained for further studies including mathematical modeling.

Next, the model-predicted mixed-reactant fuel cell polarization curves and comparison with experimental results are discussed. Our main interest with this preliminary modeling and validation study was to assess the capability of the model to predict the open circuit potential in the MRFC and to evaluate the effect of the
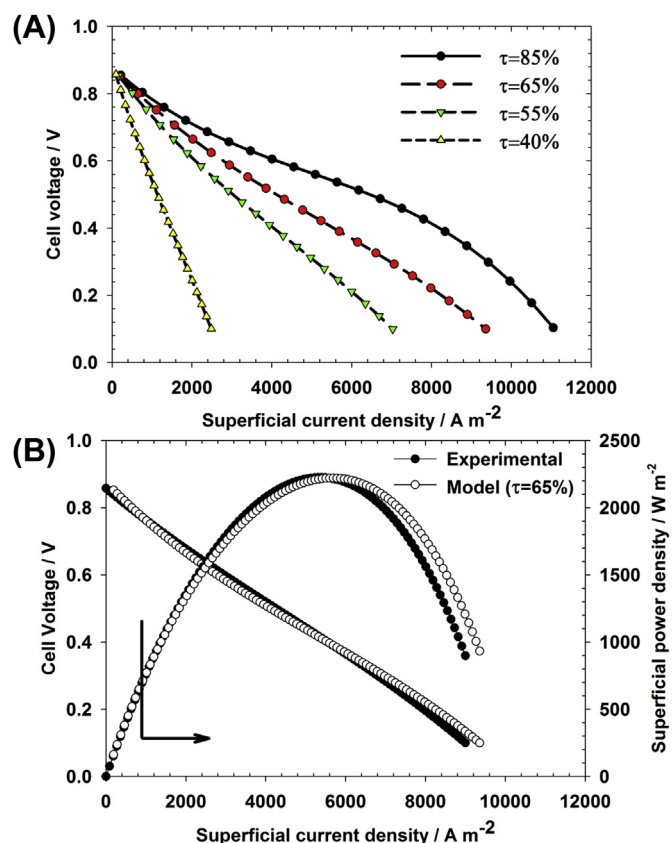
cathode hydrophilic pore volume fraction τ on the polarization performance. The latter parameter is difficult to be measured independently. The cathode hydrophilic volume fraction has two main opposing effects: i) a higher τ increases the effective ionic conductivity of the cathode, thereby, lowers the cathode Ohmic potential loss, and ii) the higher τ the more impeded is the O₂ gas mass transfer to the cathode.

Fig. 8(A) shows that based on model predictions the hydrophilic pore volume fraction in the MnO₂ cathode GDE, has a significant influence on the SR-MRFC polarization. As τ increases from 40% to 85%, the cell performance improves markedly (Fig. 8(A)), e.g., at 0.4 V for $\tau = 40\%$ the current density is about 2000 A m⁻², whereas at $\tau = 85\%$ the current density is 8125 A m⁻². Thus, our simulation results confirm that the cathodic Ohmic potential losses represent a significant portion of the total potential losses. In case of the conventional DBFC architecture as well, both modeling reports [12] and experimental observations with either O₂ or H₂O₂ oxidants [38–40] emphasized the role of the Ohmic potential losses in controlling the borohydride fuel cell polarization behavior.

At $\tau = 85\%$ the mass transfer limited region of the polarization curve is noticeable due to hampered O₂ mass transfer as a result of cathode flooding. Comparing the experimental results with model predictions a very good fit is obtained for $\tau = 65\%$ (Fig. 8(B)). The role of partial cathode hydrophilicity has been experimentally observed in case of a novel, selective, ORR catalyst layer using Fe-aminoantipyrine (Fe-AApyr) [6,7]. Thus, the present preliminary mathematical model based on mixed potential theory should be further developed and refined by carrying out a sensitivity analysis accompanied by experimental validation with respect to other
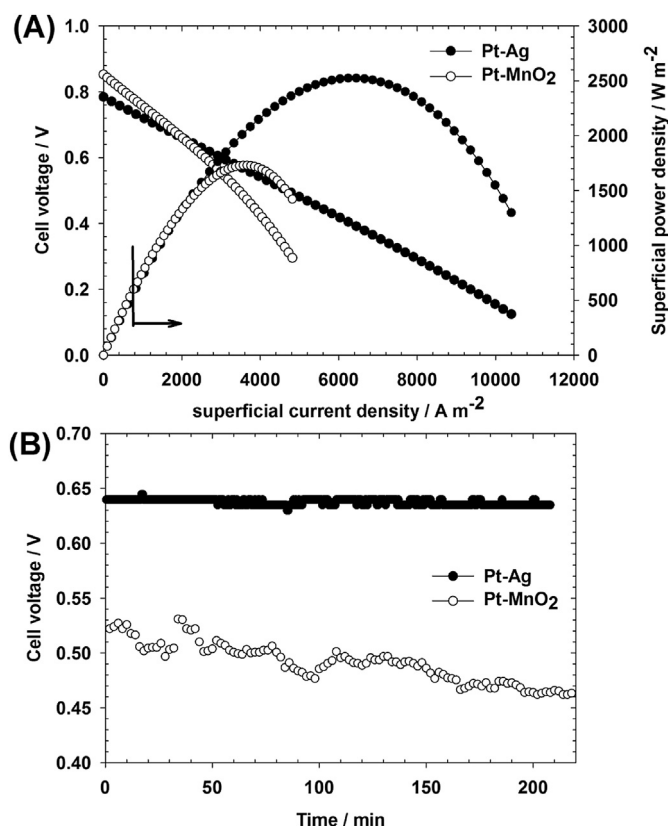
Fig. 9. (A) Effect of the cathode catalyst on the SR-MRFC polarization performance. (B) Short-term durability under galvanostatic operation at 2500 A m^{-2}. Cathode: teflonated GDE with either MnO_2 or Ag catalyst. Separator: Viledon$^{®}$; Pt/C anode. Other conditions as in http://www.sciencedirect.com/science/article/pii/ S0378775312006672 Fig. 6.

important variables such as: BH_4^- and OH^- concentration, temperature, O_2 and electrolyte flow rates, pressure, separator thickness, etc. These are the focus of our ongoing research program in this area together with developing a more comprehensive model considering axial and radial distributions of concentration, temperature, potential and current.

Next, the cathode catalyst effect (i.e. MnO_2 vs. Ag) is investigated both on the short-term polarization performance and durability during galvanostatic operation (Fig. 9). In principle, Ag is not an intrinsically selective catalyst for ORR because it can act as a BH_4^- electro-oxidation catalyst [41]. However, as shown by Fig. 9(A), in spite of the lower OCV the maximum superficial power density of the cell with the Ag gas-diffusion cathode is about 47% higher than with MnO_2, under otherwise identical conditions (e.g., both cells utilized the fine mesh (#40) cathode fluid distributor). This is due to the superior ORR kinetics on Ag compared to MnO_2 in alkaline media. The electrode kinetic region of the polarization curves in Fig. 9(A) suggests lower ORR Tafel slope in case of Ag cathode catalyst. Another benefit of the Ag cathode can be observed in Fig. 9(B), regarding performance durability during continuous galvanostatic polarization at 2500 A m^{-2}. In case of the Ag cathode catalyst, the cell voltage was virtually constant throughout the 220 min test time. In other words, the cell voltage drop was below the detection limit of the instrument (i.e. 100 µV voltage measurement precision), implying that the cell voltage drop was lower than about 27 µV h^{-1}. For the MnO_2 gas-diffusion cathode however, the voltage drop was much more significant, around 7 mV h^{-1} (Fig. 9(B)). This result suggests MnO_2 cathode degradation as the major failure mode of the SR MRFC. The performance

degradation of the MnO_2 as an ORR catalyst has been previously documented in the literature and ways to extend the stability of the catalyst are being investigated [42]. A thorough analysis of the SR-MRFC degradation using various accelerated degradation protocols was beyond the objective here and will also constitute the focus of our further studies. Depending on the intended commercial application, durability has to be demonstrated for 5000 to 20,000 h of continuous operation with a degradation rate of only a few µV h^{-1}.

5. Conclusion

The performance of the Swiss-roll single-cell mixed-reactant (SR-MRFC) borohydride fuel cell equipped with Pt/carbon cloth anode coupled with either MnO_2 or Ag gas-diffusion cathode was investigated by a combination of experimental studies and preliminary mathematical modeling. The experimental goal here was to further improve the cell performance compared to the results already reported by us [1,2] by investigating two engineering design variables: i) the cathode fluid distributor stainless steel fine mesh # 40 vs. expanded mesh # 6 and ii) the separator type, namely cation exchange membrane Nafion$^{®}$-112 vs. Viledon$^{®}$ porous unselective diaphragm.

Using the expanded mesh (mesh # 6) fluid distributor on the cathode side, a Viledon$^{®}$ separator and a MnO_2 gas-diffusion cathode with a hydrophilic pore volume fraction of 65% (determined by comparing model predictions with experimental results) we report a maximum superficial power density of 2230 W m^{-2} for the SR-MRFC operated at 323 K, 105 kPa(abs) using a two-phase spray feed composed of 1 M $NaBH_4$ − 2 M NaOH and O_2 gas. The latter superficial power density is almost 3.5 times higher than our previously reported peak superficial power density (640 W m^{-2}) obtained with the Pt−MnO_2 anode−cathode electrocatalyst combination in the SR-MRFC but equipped with the fine mesh (mesh # 40) cathode fluid distributor and two-layers of Scimat$^{®}$ separator [2]. Clearly, the two-phase flow dynamics in the porous fluid distributor and the effective Ohmic potential drop across the separator layer have a significant influence on cell performance.

Briefly, the larger pores in the expanded mesh cathode-side fluid distributor have a lower gas breakthrough pressure based on the Laplace equation, hence, the cathode is preferentially supplied by oxygen gas as opposed to liquid electrolyte. Regarding the separator, electrochemical impedance spectroscopy of the SR-MRFC demonstrated the major advantages for ionic transport when Viledon$^{®}$ separator is used compared to the cell equipped with Nafion$^{®}$-112.

Lastly, the short-term polarization performance and the durability during galvanostatic polarization improved considerably when the MnO_2 gas-diffusion cathode was replaced by Ag gas-diffusion cathode. Thus, with the Pt−Ag anode−cathode electrocatalyst combination the maximum superficial power density was 2500 W m^{-2} at 323 K when using the expanded mesh # 40 cathode fluid distributor. Furthermore, during 220 min of continuous testing at a constant current density of 2500 A m^{-2}, with the Ag gas diffusion cathode the SR-MRFC voltage drop was undetectable within the precision of our instrument, i.e., less than 100 µV voltage drop in 220 min (or less than 27 µV h^{-1}). For comparison, under identical conditions the cell equipped with the MnO_2 gas-diffusion cathode exhibited a cell voltage drop of about 7 mV h^{-1}. The promising durability results with the Ag gas-diffusion cathode warrant further investigations using accelerated durability testing protocols (e.g., diverse current or voltage cycling protocols, including voltage reversal situations as well, various operating temperatures and start-up/shut-down cycles).

In addition to the experimental studies a preliminary mathematical model is presented describing the electrode kinetics using mixed-potential theory, while also considering Ohmic losses and mass transport overpotentials. With this model we were able to simulate for the first time the polarization curve of the SR-MRFC for one set of conditions revealing, by sensitivity analysis, the role of the cathode hydrophilic volume fraction. The model presented in this work is highly simplified, and its usefulness with regard to practical cell design is limited. Improvement and extension of the model by considering composition, temperature, potential and current gradients, accompanied by two-phase flow fluid dynamics visualization studies in the Swiss-roll and experimental validation by fuel cell experiments is currently the focus of our research program and will be presented in our future publications.

Acknowledgment

References

[1] A. Aziznia, C.W. Oloman, E.L. Gyenge, ChemSusChem 6 (2013) 847–855.
[2] A. Aziznia, C.W. Oloman, E.L. Gyenge, J. Power Sources 212 (2012) 154–160.
[3] a) C. W. Oloman, Br. Pat. GB 2474202 2012.
    b) C.W. Oloman, E. Gyenge and A. Aziznia, USPTO 61869053, August 23, 2013.
    c) A. Aziznia, Ph.D. Thesis, The University of British Columbia, Vancouver, Canada, 2013.
[4] D.M.F. Santos, C.A.C. Sequeira, Renew. Sustain. Energy Rev. 15 (2011) 3980–4001.
[5] J. Ma, N.A. Choudhury, Y. Sahai, Renew. Sustain. Energy Rev. 14 (2010) 183–199.
[6] A.A. Serov, A. Aziznia, H.P. Benhangi, K. Artyushkova, P. Atanassov, E.L. Gyenge, J. Mater. Chem. A 1 (2013) 14384–14391.
[7] A. Aziznia, P.H. Benhangi, A. Serov, P. Atanassov, C.W. Oloman, E. Gyenge, in: ECS 224th Meeting, San Francisco, USA, 2013. Abstr. 1385.
[8] Freudenberg Nonwovens, Viledon® FS2227E Technical Data Sheet, 2011.
[9] A.K. Shukla, C.L. Jackson, K. Scott, G. Murgia, J. Power Sources 111 (2002) 43–51.
[10] A.E. Sanli, M.L. Aksu, B.Z. Uysal, Int. J. Hydrogen Energy 36 (2011) 8542–8549.
[11] A. Verma, S. Basu, J. Power Sources 168 (2007) 200–210.
[12] A.A. Shah, R. Singh, C. Ponce de León, R.G. Wills, F.C. Walsh, J. Power Sources 221 (2013) 157–171.
[13] B.H. Liu, S. Suda, J. Power Sources 164 (2007) 100–104.
[14] D.A. Finkelstein, N. Da Mota, J.L. Cohen, H.D. Abruña, J. Phys. Chem. C 113 (2009) 19700–19712.
[15] B. Molina Concha, M. Chatenet, E.A. Ticianelli, F.H.B. Lima, J. Phys. Chem. C 115 (2011) 12439–12447.
[16] M.C.S. Escaño, E. Gyenge, R.L. Arevalo, H. Kasai, M. Clare, S. Esca, J. Phys. Chem. C 115 (2011) 19883–19889.
[17] V.W.S. Lam, D.C.W. Kannangara, A. Alfantazi, E.L. Gyenge, J. Phys. Chem. C 115 (2011) 2727–2737.
[18] V.W.S. Lam, A. Alfantazi, E.L. Gyenge, J. Appl. Electrochem. 39 (2009) 1763–1770.
[19] G. Rostamikia, M.J. Janik, Energy Environ. Sci. 3 (2010) 1262.
[20] R.L. Arevalo, M.C.S. Escaño, E. Gyenge, H. Kasai, Surf. Sci. 606 (2012) 1954–1959.
[21] A. Ignaszak, D.C.W. Kannangara, V.W.S. Lam, E.L. Gyenge, J. Electrochem. Soc. 160 (2012) H47–H53.
[22] K. Scott, W.M. Taama, P. Argyropoulos, J. Power Sources 79 (1999) 43–59.
[23] F. Walsh, A First Course in Electrochemical Engineering, The Electrochemical Consultancy, Romsey, England, 1993.
[24] C.W. Oloman, Electrochemical Processing for the Pulp & Paper Industry, The Electrochemical Consultancy, Romsey, England, 1996.
[25] S.G. Bratsch, J. Phys. Chem. Ref. Data 18 (1989) 1.
[26] D.D. Wagman, W.H. Evans, V.B. Parker, R.H. Schumm, I. Halow, J. Phys. Chem. Ref. Data 11 (1982).
[27] B. Molina Concha, M. Chatenet, Electrochim. Acta 54 (2009) 6130–6139.
[28] M. Chatenet, M.B. Molina-Concha, N. El-Kissi, G. Parrour, J.-P. Diard, Electrochim. Acta 54 (2009) 4426–4435.
[29] K. Scott, W.M. Taama, S. Kramer, P. Argyropoulos, K. Sundmacher, Electrochim. Acta 45 (1999) 945–957.
[30] E.H. Yu, K. Scott, R.W. Reeve, Fuel Cells 3 (2003) 169–176.
[31] a) M. Chatenet, F. Micoud, I. Roche, E. Chainet, J. Vondrák, Electrochim. Acta 51 (2006) 5452–5458;
    b) A.C. Garcia, F.H.B. Lima, E.A. Ticianelli, M. Chatenet, J. Power Sources 222 (2013) 305–312.
[32] B. Šljukić, D.M.F. Santos, C.A.C. Sequeira, J. Electroanal. Chem. 694 (2013) 77–83.
[33] E. Gyenge, J.F. Drillet, J. Electrochem. Soc. 159 (2012) F23–F34.
[34] X. Yang, Y. Liu, S. Li, X. Wei, L. Wang, Y. Chen, Sci. Rep. 2 (2012) 567.
[35] F. Bidault, D.J.L. Brett, P.H. Middleton, N. Abson, N.P. Brandon, Int. J. Hydrogen Energy 35 (2010) 1783–1788.
[36] F. Bidault, D.J.L. Brett, P.H. Middleton, N.P. Brandon, J. Power Sources 187 (2009) 39–48.
[37] Z. Samec, A. Trojánek, J. Langmaier, J. Electrochem. Soc. 145 (1998) 2740.
[38] B.H. Liu, Z.P. Li, K. Arai, S. Suda, Electrochim. Acta 50 (2005) 3719–3725.
[39] B.H. Liu, Z.P. Li, J.K. Zhu, S. Suda, J. Power Sources 183 (2008) 151–156.
[40] R.K. Raman, A.K. Shukla, Fuel Cells 7 (2007) 225–231.
[41] M.H. Atwan, D.O. Northwood, E.L. Gyenge, Int. J. Hydrogen Energy 32 (2007) 3116–3125.
[42] P.H. Benhangi, A. Alfantazi, E.L. Gyenge, Electrochim. Acta 123 (2013) 42–50.